Simulation of reduction of oxidized metal nanoparticles

N.B. When citing this work, cite the original published paper.

(article starts on next page)

Simulation of reduction of oxidized metal nanoparticles

Vladimir P. Zhdanov[1,2]

Abstract

I analyze theoretically the spatio-temporal kinetics of reduction of oxidized metal nanoparticles by hydrogen (or methane). The focus is on the experimentally observed formation of metal and oxide domains separated partly by pores. The interpretation of such multiphase processes in nanoparticles at the mean-field level is hardly possible primarily due to complex geometry, and accordingly I use the lattice Monte Carlo technique in order to tackle this problem. The main conclusions drawn from the corresponding generic simulations are as follows. (i) The patterns predicted are fairly sensitive to the metal-metal and metal-oxygen interactions. With decreasing the former interaction and increasing the latter interaction, there is transition from the formation of metal aggregates and voids to the formation of a metal film around the oxide core. (ii) During the initial phase of these kinetics, the extent of reduction can roughly be described by using the power law, and the corresponding exponent is about 0.3. (iii) With decreasing the hydrogen (or methane) pressure and/ or increasing the oxide nanoparticle size, as expected, the kinetics are predicted to become longer. (iv) The dependence of the patterns on the presence of the support and/or Kirkendall void in an oxide nanoparticle is shown as well.

Keywords Metal · Oxide · Nanopartiles · Phase separation · Kinetics · Model · Monte Carlo simulations

Introduction

Metal nanopartiles (MNPs) have long been in the center of heterogeneous catalysis [1] and are now in the center of nanoscience in general with numerous potential and already realized applications (reviewed e.g. in [2, 3]). In reality, MNPs tend to deteriorate. In catalysis under relatively high temperatures, it often occurs via sintering (reviewed in [4–6]). In other applications, at lower temperatures, the

✉ Vladimir P. Zhdanov
  zhdanov@chalmers.se; zhdanov@catalysis.ru

1   Department of Physics, Chalmers University of Technology, Göteborg, Sweden

2   Boreskov Institute of Catalysis, Russian Academy of Sciences, Novosibirsk, Russia

⊘ Springer

deterioration of MNPs is frequently related to their oxidation, i.e., conversion to oxide NPs (ONPs; see e.g. recent reviews [7, 8], experiments [9–12], kinetic models [13, 14], and references therein). The metal properties of ONPs can be restored at least partly by reduction via reaction with hydrogen (or methane) as reviewed in [15] (for recent experiments, see also e.g. [16–19]). The available mean-field kinetic models of reduction of ONPs imply the formation of a core-shell NP structure (see e.g. [20–23]). In reality, this process can be more complex. For NiO NPs, for example, the experiments indicate that the reduction is accompanied by the formation of metal and oxide domains separated partly by pores [15, 24]. The description of such processes at the mean-field level is hardly possible primarily due to complex geometry. The full-scale Monte Carlo (MC) simulations are also hardly possible due to the uncertainty with the choice of numerous parameter and large values of metal-metal and metal-oxygen interactions, and the corresponding models are now lacking. Herein, I present the first generic 2D lattice MC simulations illustrating the key features of phase separation during reduction of ONPs.

From the perspective of statistical physics, the process under consideration is a special case of phase separation under reactive conditions. Other examples of processes belonging to this class are available in heterogeneous catalysis, and the corresponding models are generic as well (see e.g. MC simulations [25, 26]). The specifics of phase separation during reduction of ONPs and in heterogeneous catalytic reactions are, however, fairly different.

Model

The simulations are performed on a square $L \times L$ lattice. Each site can be occupied by one monomer, A (metal), B (oxygen), or C (mimic of hydrogen), or be vacant. An ONP is represented at $t = 0$ by a square $c(2 \times 2)$ $l \times l$ A-B array (see, e.g., Fig. 1). The other sites are initially (at $t = 0$) assumed to be vacant or occupied by C with probability $p < 1$ (this parameter is related to hydrogen pressure). The analysis

Fig. 1 Central 160×130 fragment of the 200×200 lattice showing a typical initial $c(2 \times 2)$ 100×100 distribution of A (filled circles representing metal atoms) and B (open circles representing oxygen atoms)
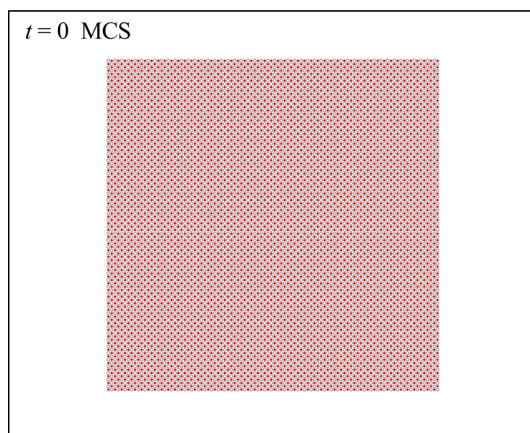
includes diffusion of A, B, and C via jumps to nearest-neighbour (nn) vacant sites. These jumps are schematically represented as

$$R + Z \rightarrow Z + R, \tag{1}$$

where R is A, B, or C, and Z is a nn vacant site. In addition, there is irreversible reaction between reactants located in nn sites,

$$B + C \rightarrow \varnothing. \tag{2}$$

The driving force for the oxide formation is described by introducing the attractive nn interaction, $\epsilon_{AB} < 0$, between nn A and B. The tendency of metal atoms to aggregate is reflected by introducing the attractive nn A-A interaction, $\epsilon_{AA} < 0$. The other interactions (ϵ_{AC}, ϵ_{BB}, ϵ_{BC}, and ϵ_{CC}) are neglected.

In the framework of the transition state theory, the rate constant of a monomer jump to a nn vacant site is determined by the pre-exponential factor and the activation energy identified as usual with the difference of the monomer energies in the activated state, i.e., at the saddle points of the potential barriers, and in the ground state, i.e., near the bottom of potential wells [27] (for the other dynamics, see e.g. [28]). A monomer performing a jump interacts laterally (in the 2D case) with neighbours, which are in the ground state. Depending on the location of a jumping monomer, there are lateral interactions in the ground and activated states, $\epsilon_{X,i}$ and $\epsilon_{X,i}^*$, where X is the subscript characterizing the monomer type (X $\equiv$ A, B, or C), and i is the subscript characterizing the arrangement of neighbours. The difference of these energies determines the contribution of lateral interactions to the jump activation energy. To reduce the number of parameters, the lateral interaction in the activated states are here neglected, i.e., $\epsilon_{X,i}^* = 0$. The lateral interaction in the ground state is reduced to the nn interactions as described above. With this specification, the rate constants of a A, B, or C jump in one of the directions are represented as

$$\begin{aligned}
k_{A,i} &= k_A^\circ \exp[(n\epsilon_{AA} + m\epsilon_{AB})/k_B T], \\
k_{B,i} &= k_B^\circ \exp(m\epsilon_{AB})/k_B T), \\
k_{C,i} &= k_C^\circ,
\end{aligned} \tag{3}$$

where k_A°, k_B°, and k_C° are the maximal values of the rate constants, and n and m are the numbers of neighbours corresponding to a jumping A or B monomer and given i.

For MC simulations, one needs dimensionless probabilities ($p_i \leq 1$) of possible events. To get such probabilities, the rate constants are usually normalized to a properly chosen rate constant which is larger than or equal to the rate constants of all the possible events. After such normalization, expressions (3) can be replaced by

$$\begin{aligned}
p_{A,i} &= p_A^\circ \exp[(n\epsilon_{AA} + m\epsilon_{AB})/k_B T], \\
p_{B,i} &= p_B^\circ \exp(m\epsilon_{AB}/k_B T), \\
p_{C,i} &= p_C^\circ,
\end{aligned} \tag{4}$$

where $p_A^\circ \le 1$, $p_B^\circ \le 1$, and $p_C^\circ \le 1$ are the jump probabilities in the absence of neighbours.

Reaction (2) is considered to be fast, i.e., to occur just after a diffusion jump of B (or C) if it has one or more nn C (or B). If after a diffusion jump of B (or C) it has more than one nn C (or B), the second reactant is chosen at random.

On the lattice boundary, the no-flux boundary condition are employed for A and B, i.e., the jumps of these monomers out of the lattice are not allowed. The C supply to the lattice is mimicked by using for this species the grand canonical distribution with the prescribed average C population, p (as at $t = 0$), on the border sites during trials of C jumps from the boundary sites to the interior of the lattice or from the interior to the boundary.

Algorithm of simulations

With the specification above, the algorithm of MC simulations is as follows:

(i)   A site is chosen at random.
(ii) If the site chosen is vacant, a trial ends.
(iii) If the site chosen is occupied, a monomer located in this site tries to diffuse [step (1)]. In particular, a nn site is randomly selected, and if the latter site is vacant, the monomer jumps to it with probability $p_{A,i}$, $p_{B,i}$, or p_C° [Eq. (4)].
(iv) After a B (or C) jump, the nn sites are inspected and if these sites contain at least one C (or B), B (or C) reacts [step (2)] with randomly selected C (or B).
(v)   After each MC trial, the dimensionless time is incremented by $\Delta t = |\ln(\rho)|/L^2$, where $0 < \rho \le 1$ is a random number.

The jumps near and at the boundary sites are simulated with the specification described in the end of Sec. 2.

On average, $\Delta t = 1$ corresponds to L^2 MC trials. In the simulations presented, as usual, $\Delta t = 1$ is identified with one MC step (MCS). To convert t into real time, it should be divided by the rate constant which was used for normalization of the jump rate constants. The simulations are, however, focused on the patterns arising during reduction of ONPs, and from this perspective the time units are not important. For this reason, the time is below given in MCS.

MC runs were performed on a lattice with $L = 200$ up to $t = 10^7$ MCS. The size of the A+B array at $t = 0$ was $l = 100$ or 70. The kinetics observed were characterized by calculating the extent of reduction,

$$\varphi(t) = 1 - n_B(t)/n_B(0), \tag{5}$$

where $n_B(t)$ and $n_B(0) \equiv l^2/2$ are the current and initial B populations.

Results of simulations

In the model presented, the jump probabilities defined by (4) depend on p_A°, p_B°, p_C°, and the ratios $\epsilon_{AA}/k_B T < 0$ and $\epsilon_{AB}/k_B T < 0$. In reality, the absolute values of these ratios are large ($\gg 1$), and with their realistic values MC simulations are too slow. For this reason, the use of relatively small absolute values of these ratios is usually inevitable. With this reservation, the bulk of the MC simulations shown below was performed with $\epsilon_{AA}/k_B T = -4$ and $\epsilon_{AB}/k_B T = -3$. To make the simulations faster, the diffusion jumps were run with $p_A^\circ = p_B^\circ = p_C^\circ = 1$.

To illustrate the predicted reduction kinetics and the corresponding patterns, I present 6 MC runs with different sets of parameters or initial conditions. Run 1 was performed with $L = 200$, $l = 100$, $p = 0.1$, $\epsilon_{AA}/k_B T = -4$, and $\epsilon_{AB}/k_B T = -3$. Initially, the A-B array was located in the center (Fig. 1). In Runs 2-6, one or two of these parameters or the initial conditions are changed in order to show the sensitivity of the results with respect to such changes. In particular, the initial arrangements were without vacant sites inside (as in Fig. 1) in Runs 1-5 and with an array of vacant sites in Run 6.

The reduction kinetics corresponding to Runs 1-5 are exhibited in Fig. 2. During the initial phase of these kinetics, the extent of reduction defined by (5) can roughly be described by using the power law,

$$\varphi(t) \propto t^\alpha, \tag{6}$$

with $\alpha \simeq 0.3$. This exponent is close to the Lifshitz-Slyozov exponent, $\alpha_{LS} = 1/3$, for Ostwald ripening (see e.g. [29, 30]). This coincidence is natural because the reduction occurs in parallel and is influenced by the growth of A aggregates. More specifically, the analysis of the kinetics shown in Fig. 2 indicates that $\alpha = 0.32$ for Run 1, 0.21 for Run 2, 0.51 for Run 3, 0.31 for Run 4, and 0.33 for Run 5. The
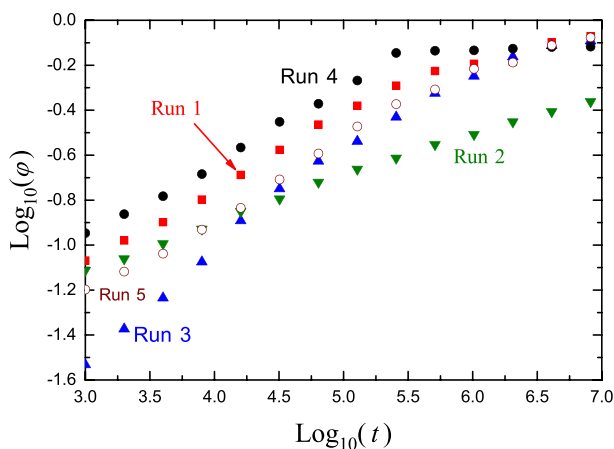

Fig. 2 Extent of conversion [Eq. (5)] of the initial distribution of A and B as a function of time (in the logarithmic coordinates) during five MC runs predicted by the model under various conditions

deviations of α from 0.3 are seen to be maximal in the cases of Runs 2 and 3. The related remarks are given below together with the discussion of the corresponding patterns.

Typical patterns observed during MC simulations with the first set of the parameters (Run 1) are shown in Fig. 3. The A aggregates and voids are seen to be rather small up to $t = 10^4$ MCS [Fig. 3a]. With increasing time, the A aggregates and voids grow and at $t = 10^7$ MCS [Fig. 3d] their size becomes to be comparable with the initial size of the A-B array.

Regarding the variation of parameters, it is of interest to notice that the results of the simulations are fairly sensitive to the values of the ratios $\epsilon_{AA}/k_B T$ and $\epsilon_{AB}/k_B T$. This is illustrated by using the second set of the parameters with $\epsilon_{AA}/k_B T = -3$ and $\epsilon_{AB}/k_B T = -4$ (Run 2, Fig. 4). With decreasing $|\epsilon_{AA}/k_B T|$ and increasing $|\epsilon_{AB}/k_B T|$ (compared to that in the first set of the parameters), the driving force for the A segregation becomes weaker, i.e., the relative stability of the A-B phase increases, and the model predicts formation of the A layer around the A-B core (Fig. 4), and the whole kinetics becomes slower compared to that
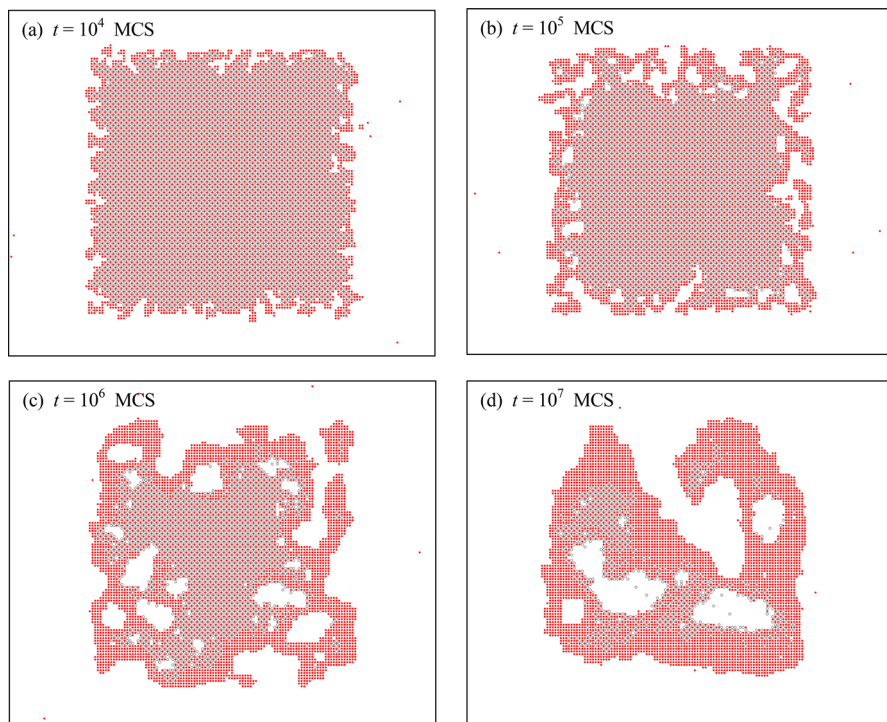

Fig. 3 Central 160×130 fragment of the 200×200 lattice during Run 1 (Fig. 2) with $L = 200$, $l = 100$, $p = 0.1$, $\epsilon_{AA}/k_B T = -4$, and $\epsilon_{AB}/k_B T = -3$, at $t = 10^4$ (a), 10^5 (b), 10^6 (c), and 10^7 MCS (d). A (metal) and B (oxygen) monomers are shown by filled and open circles, respectively. The C monomers (mimic of hydrogen) are not indicated
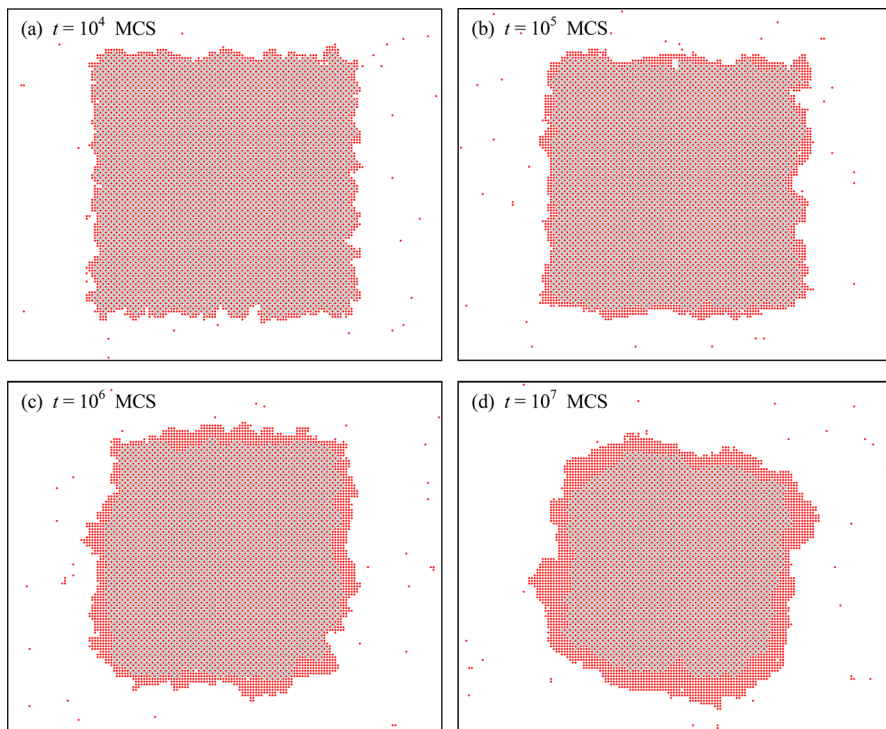
Fig. 4 As Fig. 3 for Run 2 (Fig. 2) with $\epsilon_{AA}/k_B T = -3$ and $\epsilon_{AB}/k_B T = -4$ (the other parameters are as for Run 1 shown in Fig. 3)

observed during Run 1 (Fig. 2). One of the manifestation of this A-layer-related slowdown is that α is reduced down to 0.21.

The main goal of the work was to show the A segregation and void formation, and the first set of parameters (Run 1) was selected from this perspective. The other simulations presented below were performed with the same values of the ratios $\epsilon_{AA}/k_B T$ and $\epsilon_{AB}/k_B T$ as in the first set of parameters. In particular, the third set of the parameters (Run 3) was chosen as the first one except the p value which was reduced from 0.1 to 0.02. In reality, this physically corresponds to decrease of the hydrogen pressure. With this modification, as expected, the kinetics becomes slower than during Run 1 (Fig. 2). The patterns are, however, qualitatively similar to those observed in Run 1 (cf. Figure 3 and S1 in Supplementary Information), i.e., there is no formation of the coherent A film in the external area of the array. For this reason, this slowdown of the kinetics does not reduce α (as in the case of Run 2). In fact, α increases up to 0.51, because B particles have more time to diffuse from the internal area to the external area and react there.

In the fourth set of the parameters (Run 4), l was reduced from 100 to 70. With this modification, the kinetics becomes shorter (see Fig. 2 and cf. Figures 3 and S2 in Supplementary Information).

The fifth set of the parameters (Run 5) was identical to the first one. The difference was in the initial conditions with one of the side of the A-B array contacting one of the lattice boundaries and prohibition of C supply at this boundary. These boundary conditions are aimed to simulate an oxide nanoparticle located at the support. In this case, the kinetics is somewhat slower than during Run 1 (Fig. 2), and the reduction occurs primarily in the upper part of the array (Fig. 5).

The sixth set of the parameters (Run 6) was identical to the first one as well, and the difference was also in the initial conditions. Here, the initial 100×100 A-B array had inside a circular region of vacant sites. The radius of this region was 30. These initial conditions are aimed to simulate an ONP with a void inside. Such ONPs are often observed in experiments after oxidation of MNPs and associated either with the specifics of diffusion of metal atoms and oxygen (Kirkendall effect [31, 32]) and/or induction of tensile strain [33, 34] during oxidation. With this setup, the initial phase of the kinetics and the corresponding patterns are similar to those predicted with the first set of the parameters (cf. Figures 3 and S3 in Supplementary Information). After penetration of C to the central region, the kinetics becomes, however, faster, and there is difference in the patterns.
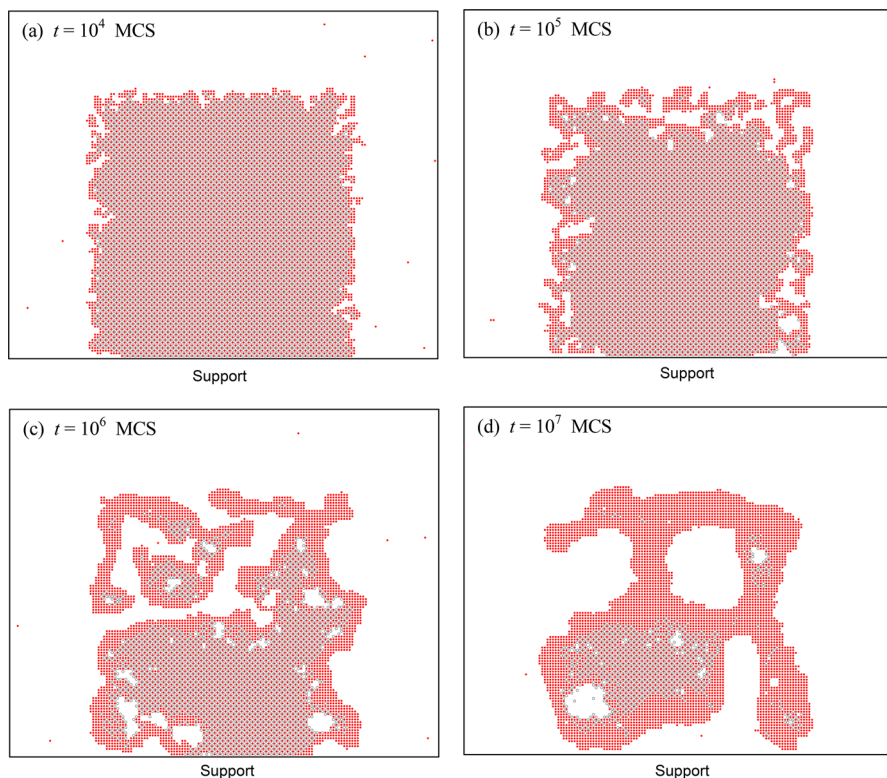

Fig. 5 As Fig. 3 for Run 5 (Fig. 2) with the same parameters as for run 1 shown in Fig. 3. Here, the A-B array contacts the lattice boundary

Conclusion

The MC simulations performed in the framework of the proposed generic 2D lattice model on the times up to 10^7 MCS illustrate the specifics of the formation of metal aggregates and voids during reduction of OMNs by hydrogen or methane. This duration of the MC runs is sufficient in order to reach appreciable extent of reduction. The conclusions drawn from the simulations are as follows:

(i) As one could expect physically, the patterns observed in the simulations are fairly sensitive to the A-A (metal-metal) and A-B (metal-oxygen) interactions. With decreasing the former interaction and increasing the latter interaction, the model predicts the transition from the formation of metal aggregates and voids to the formation of a metal film around the oxide core. This effect was not obvious in advance and accordingly can be classified as novel.

(ii) During the initial phase of the kinetics under consideration, the extent of reduction can roughly be described by using the power law with $\alpha \simeq 0.3$. This finding is novel as well.

(iii) With decreasing p (hydrogen or methane pressure) and/or increasing the ONP size, the kinetics become longer.

(iv) The patterns depend on the presence of the support and/or Kirkendall void in an ONM.

All these conclusions obtained in the framework of the 2D lattice model appear to be physically reasonable, and one can add that two of them, (iii) and (iv), are obvious and applicable in the 3D case as well. The other two, (i) and (ii), are, however, not trivial and merit additional more specific remarks. In particular, conclusion (i) is qualitative, could be physically expected, and likely holds in the 3D case. Conclusion (ii) is quantitative and physically supported by referring to the specifics of Ostwald ripening and the corresponding Lifshitz-Slyozov exponent which is applicable in the 2D and 3D cases. With this reservation, one cannot, however, exclude that in the 3D case the exponent for the ONP reduction will be somewhat different compared to the obtained one, $\alpha \simeq 0.3$. In fact, the difference has been observed in the simulations presented ($\alpha = 0.21$ for Run 2, and $\alpha = 0.51$ for Run 3).

Taken together, the results of the simulations are instructive. In particular, one can see that the qualitative interpretation of the specifics of the formation of metal aggregates and voids during reduction of ONPs by hydrogen or methane is possible at the generic level.

Finally, it is worth to notice that the model presented can be extended in various directions. One of the extensions is to choose the parameters so that the patterns become to be closer to those implied in the mean-field treatments mentioned in the Introduction. Another and perhaps more interesting extension is to perform simulations in the 3D case.

Data availability The data presented in this study are available in the article.

Code availability Not applicable.

Declarations

Conflict of interest The author declares no competing interests.

Ethical approval Not applicable.

References

1. van Santen R (2017) Modern heterogeneous catalysis: an introduction. Wiley, Weinheim
2. Mulvaney P, Buriak JM, Chen X, Hu T (2022) Nanoscience and entrepreneurship. ACS Nano 16:6943–6944
3. Bayda S, Adeel M, Tuccinardi T, Cordani N, Rizzolio F (2020) The history of nanoscience and nanotechnology: from chemical-physical applications to nanomedicine. Molecules 25:112
4. Rahmati M, Safdari MS, Fletcher TH, Argyle MD, Bartholomew CH (2020) Chemical and thermal sintering of supported metals with emphasis on cobalt catalysts during Fischer-Tropsch synthesis. Chem Rev 120:4455–4533
5. Lai KC, Han Y, Spurgeon P, Huang W, Thiel PA, Liu DJ, Evans JW (2019) Reshaping, intermixing, and coarsening for metallic nanocrystals: nonequilibrium statistical mechanical and coarse-grained modeling. Chem Rev 119:6670–6768
6. Deng S, Qiu C, Yao Z, Sun X, Wei Z, Zhuang G, Zhong X, Wang J-G (2019) Multiscale simulation on thermal stability of supported metal nanocatalysts. WIREs Comput Mol Sci. https://doi.org/10.1002/wcms.1405
7. Wang X, Feng J, Bai Y, Zhang Q, Yin Y (2016) Synthesis, properties, and applications of hollow micro-/nanostructures. Chem Rev 116:10983–11060
8. Zhang X, Zheng P, Ma Y, Jiang Y, Li H (2022) Atomic-scale understanding of oxidation mechanisms of materials by computational approaches: a review. Mater Design 217:110605
9. Bugaev AL, Zabilskiy M, Skorynina AA, Usoltsev OA, Soldatov AV, van Bokhoven JA (2020) In situ formation of surface and bulk oxides in small palladium nanoparticles. Chem Commun 56:13097–13100
10. Song B et al (2020) In situ oxidation studies of high-entropy alloy nanoparticles. ACS Nano 14:15131–15143
11. Fang Y et al (2021) Effects of oxidation on the localized surface plasmon resonance of Cu nanoparticles fabricated via vacuum coating. Vacuum 184:109965
12. Nilsson S, Nielsen MR, Fritzsche J, Langhammer C, Kadkhodazadeh S (2022) Competing oxidation mechanisms in Cu nanoparticles and their plasmonic signatures. Nanoscale 14:8332–8341

13. Zhdanov VP (2019) Kirkendall effect in the two-dimensional lattice-gas model. Phys Rev E 99:012132
14. Zhdanov VP (2020) Simulations of oxidation of metal nanoparticles with a grain boundary inside. Reac Kinet Mech Cat 130:685–697
15. Rukini A, Rhamdhani MA, Brooks GA, Van den Bulck A (2022) Metals production and metal oxides reduction using hydrogen: a review. J Sustain Metal 8:1–24
16. Fedorov AV, Kukushkin RG, Yeletsky PM, Bulavchenko OA, Chesalov YA, Yakovlev VA (2020) Temperature-programmed reduction of model CuO, NiO and mixed CuO-NiO catalysts with hydrogen. J Alloys Comp 844:156135
17. Geng X, Li S, Mei Z, Li D, Zhang L, Luo L (2023) Ultrafast metal oxide reduction at Pd/PdO2 interface enables one-second hydrogen gas detection under ambient conditions. Nano Research 16(1):1149–1157
18. Kharatyan SL, Chatilyan HA, Manukyan KV (2019) Kinetics and mechanism of nickel oxide reduction by methane. J Phys Chem C 123:21513–21521
19. Li J, Zhu Q, Li H (2021) Relationship between reaction and diffusion during ultrafine NiO reduction toward agglomeration fluidization. AIChE J 67:e17081
20. Zhou Z, Han L, Bollas GM (2014) Kinetics of NiO reduction by H_2 and Ni oxidation at conditions relevant to chemical-looping combustion and reforming. Intern J Hydr Energy 39:8535–8556
21. Ipsakis D, Heracleous E, Silvester L, Bukur DB, Lemonidou AA (2017) Reduction and oxidation kinetic modeling of NiO-based oxygen transfer materials. Chem Eng J 308:840–852
22. Ipsakis D, Heracleous E, Silvester L, Bukur DB, Lemonidou AA (2020) Reaction-based kinetic model for the reduction of supported NiO oxygen transfer materials by CH_4. Catal Today 343:72–79
23. Dang J, Wu Y, Lv Z, You Z, Zhang S, Lv X (2018) A new kinetic model for hydrogen reduction of metal oxides under external gas diffusion controlling condition. Intern J Refract Metals Hard Mater 77:90–96
24. Jeangros J et al (2013) Reduction of nickel oxide particles by hydrogen studied in an environmental TEM. J Mater Sci 48:2893–2907
25. Zhdanov VP (2005) Pattern formation in heterogeneous catalytic reactions with promoters and poisons. Phys Chem Chem Phys 7:2399–2402
26. Zhdanov VP, Vang RT, Knudsen J, Vestergaard EK, Besenbacher F (2006) Propagation of a reaction front accompanied by island formation: CO/Au/Ni(111). Surf Sci 600:L260–L264
27. Zhdanov VP (1991) Elementary physicochemical processes on solid surfaces. Plenum, New York
28. Manzi SJ, Ranzuglia GA, Pereyra VD (2009) One-dimensional diffusion: validity of various expressions for jump rates. Phys Rev E 80:062104
29. Huse DA (1986) Corrections to late-stage behaviour in spinodal decomposition - Lifshitz-Sllyyzov scaling and Monte-Carlo simulations. Phys Rev B 34:7845–7850
30. Zhdanov VP (1997) Island growth and phase separation in chemically reactive adsorbed overlayers. Surf Sci 392:185–198
31. Yin Y, Rioux RM, Erdonmez CK, Hughes S, Somorjai GA, Alivisatos AP (2004) Formation of hollow nanocrystals through the nanoscale Kirkendall effect. Science 304:711–714
32. Fan HJ, Gösele U, Zacharias M (2007) Formation of nanotubes and hollow nanoparticles based on Kirkendall and diffusion processes: a review. Small 3:1660–1671
33. Zhdanov VP, Kasemo B (2009) On the feasibility of strain-induced formation of hollows during hydriding or oxidation of metal nanoparticles. Nano Lett 9:2172–2176
34. Klinger L, Rabkin E (2015) On the nucleation of pores during the nanoscale Kirkendall effect. Mater Lett 161:508–510